Bandlimited Reconstruction of Multidimensional Images from Irregular Samples

Xie Xu, Wenxing Ye, and Alireza Entezari, *Member, IEEE*

Abstract—We examine different sampling lattices and their respective bandlimited spaces for reconstruction of irregularly sampled multidimensional images. Considering an irregularly sampled dataset, we demonstrate that the non-tensor-product bandlimited approximations corresponding to the body-centered cubic and face-centered cubic lattices provide a more accurate reconstruction than the tensor-product bandlimited approximation associated with the commonly-used Cartesian lattice. Our practical algorithm uses multidimensional sinc functions that are tailored to these lattices and a regularization scheme that provides a variational framework for efficient implementation. Using a number of synthetic and real data sets we record improvements in the accuracy of reconstruction in a practical setting.

Index Terms—Irregular sampling, sinc, interpolation and approximation, multidimensional signal processing.

I. INTRODUCTION

MODELING signals in the bandlimited setting has been prevalent in digital signal processing and its many diverse applications. Motivated by early applications in audio processing, the focus has primarily been on the theory of 1-D signal processing whose results can be extended to multi-dimensions by a tensor-product. While such separable, Cartesian, structures are easy to construct, there are known advantages in studying non-separable multidimensional signal processing. In this paper we investigate the problem of bandlimited reconstruction of a multidimensional image from an *irregularly sampled dataset* and study the advantages of non-separable image processing in the context of this problem.

A key development that has been foundational to the discrete-continuous model for processing bandlimited signals is the so called Whittaker-Shannon-Kotel'nikov theorem [1]. The bandlimited reconstruction formula involves a cardinal series expansion:

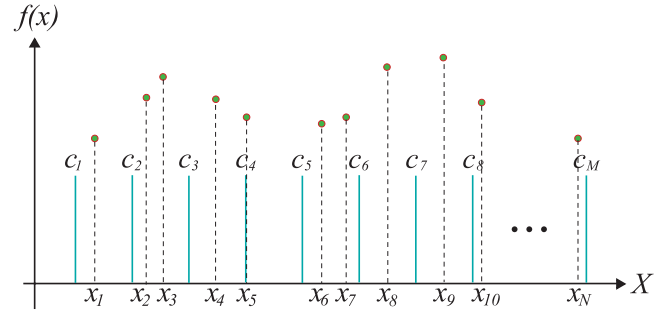$$f(x) = \sum_{k \in \mathbb{Z}} c_k \operatorname{sinc}(x - k), \qquad (1)$$

Fig. 1. Bandlimited reconstruction of 1-D signal f from N irregular samples. A uniform grid (in blue) of M unknown coefficients is imposed in the reconstruction domain and the unknown coefficients $c := \{c_1, \ldots, c_M\}$ are found from the irregular samples (the circles) located at $X := \{x_1, \ldots, x_N\}$ with signal values $f_s := \{f_1, \ldots, f_N\}$. The underlying signal f can then be obtained from the coefficients c_k using formula (1). In 2-D, the imposed uniform grid can be Cartesian or hexagonal lattice, while in 3-D, the grid can be Cartesian, BCC, or FCC lattice (see Fig. 2).

where $\operatorname{sinc}(x) := \sin(\pi x)/(\pi x)$ whose Fourier transform is the indicator function, $\chi_{(-\pi,\pi)}$, of the interval bound by the Nyquist frequency (i.e., unit cell of the periodic spectrum of the sampling lattice $\mathbb{Z}$). When f is a bandlimited function, the simple choice of function's samples on regular intervals $c_k = f(k)$ allows us to perfectly reconstruct f. In the practical setting, the sinc function is often truncated with the aid of windowing techniques (e.g., Lanczos, Hamming, Parzen, Blackman) [2] such that a finite domain reconstruction is feasible.

Generalizations of the sampling theorem have been studied in several directions. For example when the data has been sampled irregularly, results from Beurling and Landau [3] provide a theoretical framework for bandlimited reconstruction from such irregular samples (see Fig. 1). In this context, the data points $f_s = \{f_1, \ldots, f_N\}$ are given by sampling f on a non-uniform set of points $X := \{x_1, \ldots, x_N\}$, i.e., $f_n = f(x_n)$. The reconstruction process starts by imposing a (scaled and uniform) grid, of unknown c_k coefficients to sinc functions as in (1) and provides a recipe for finding c_k.

When it comes to the multivariate setting, (1) can be simply extended with a Cartesian product: the function is sampled on a Cartesian lattice (i.e., $c_{\mathbf{k}} = f(\mathbf{k})$ where $\mathbf{k} \in \mathbb{Z}^d$) and the multivariate sinc is constructed by the tensor-product of the sinc function. The Fourier transform of such a tensor-product sinc is the indicator function of a (hyper-) cube that runs $(-\pi, \pi)$ on each axis of the frequency.

While the Cartesian cubic (CC) lattice is commonly used in applications due to its simplicity, the seminal work of Miyakawa [4] and Petersen and Middleton [5] showed the
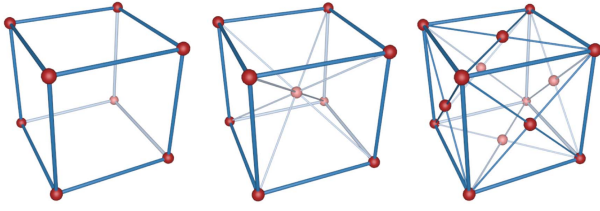
Fig. 2. Cartesian, BCC and FCC lattices.

advantages of using non-Cartesian lattices such as sphere packing lattices over the CC lattice. Particularly, the 2-D hexagonal lattice [6] and the 3-D Face Centered Cubic (FCC) and Body Centered Cubic (BCC) lattices (see Fig. 2) have been demonstrated to be superior to the CC lattice for sampling and reconstruction of isotropically bandlimited signals [5], [7], [8]. Both families of these non-Cartesian lattices outperform the efficiency of the CC lattice from the sampling-theoretic viewpoint: for general 3-D bandlimited signals to be sampled on a CC lattice, the BCC and FCC lattices allow the reduction of the sampling rate by 30% and 23% respectively [5]. This notion of efficiency increases in higher dimensions, as the efficiency is 14% for the 2-D hexagonal lattice and 50% for the 4-D checkerboard lattice [9].

A. General Lattices

A generic lattice in any dimension is the integer span of a set of basis vectors that are often arranged in a matrix, $\mathbf{L}$. The 2-D CC lattice is represented by the 2×2 identity matrix and the hexagonal lattice can be represented with $\mathbb{H} = [\mathbf{u}, \mathbf{v}]$, where $\mathbf{u} = [1/2, \sqrt{3}/2]^T$ and $\mathbf{v} = [1/2, -\sqrt{3}/2]^T$. In the 3-D setting, the CC lattice points are the span of the columns of $\mathbb{C} := \mathbf{I}$ (i.e., the 3×3 identity matrix). The FCC and BCC lattices are spanned by the columns of $\mathbb{F}$ and $\mathbb{B}$, respectively:

$$\mathbb{F} := \begin{bmatrix} 0 & 1 & 1 \\ 1 & 0 & 1 \\ 1 & 1 & 0 \end{bmatrix} \text{ and } \mathbb{B} := \begin{bmatrix} -1 & 1 & 1 \\ 1 & -1 & 1 \\ 1 & 1 & -1 \end{bmatrix}. \quad (2)$$

Counterparts to the BCC/FCC lattices in higher dimensions are studied by Conway and Sloane [9] that catalog the efficient higher dimensional lattices.

The **Voronoi cell** (aka unit or fundamental cell) of a lattice point is composed of all points in the ambient space that are closer to that lattice point than any other lattice point. All points in a lattice have Voronoi cells that are congruent to each other and hence one can refer to the Voronoi cell of a lattice unambiguously. The Voronoi cell of CC lattice is a cube, BCC is a truncated octahedron and FCC is a rhombic dodecahedron (also see Fig. 4). The *density* of a lattice, $\mathbf{L}$, is the reciprocal of the volume of its Voronoi cell, which is simply $1/|\det \mathbf{L}|$. The density of a lattice can be adjusted simply by scaling its generator matrix $\alpha \mathbf{L}$ with any $\alpha > 0$.

The *expected distance* of a randomly-chosen point in $\mathbb{R}^3$ to its closest point on the BCC/FCC lattice is smaller than its expected distance to the closest CC lattice point, when all three lattices have the same density. This notion of proximity can be demonstrated using the concept of moments the Voronoi cell of the lattice. Since the closest lattice point to any random

point in space encloses that point within its Voronoi cell (i.e., its neighborhood), the expected distance of a random point to the closest lattice point can be computed by the expected distance of a random point within the Voronoi cell of a lattice to its center. Compared to the cube (i.e., the Voronoi cell of a CC lattice), a random point inside the truncated octahedron or the rhombic dodecahedron (i.e., Voronoi cell of the BCC and FCC respectively) has a smaller expected distance to the cell's centroid, assuming these polyhedra have the same volume.

The *second moment* of the polytope P is defined as $U(P) = \int_P \|\mathbf{x}\|^2 d\mathbf{x}$, where $\|\mathbf{x}\|$ denotes ℓ_2-norm of the vector $\mathbf{x}$, that is, the Euclidean distance between point $\mathbf{x}$ and the centroid of the polytope. Provided P has a unit volume, $U(P)$ then indicates the expected squared distance of a random point inside the polytope to its centroid. According to [9], the second moments (i.e., $U(P)$) of unit area square and hexagon are 0.166666 and 0.160375, respectively. Moreover, the second moments of cube, truncated octahedron and rhombic dodecahedron, of unit volume, are 0.249999, 0.2356299, and 0.2362353, respectively. This shows that the expected distance of a random point to a CC lattice is larger than the distance to an FCC lattice which is only slightly larger than the distance to a BCC lattice.

B. Motivation and Contributions

a) Motivation: For a multidimensional signal, the shape of its spectrum determines the optimal sampling lattice for the signal. The optimal sampling lattice is obtained when its dual lattice can densely replicate the signal spectrum in an optimal way [7], [10]. With a known shape of the signal spectrum, one can compute the optimal sampling lattices for that specific signal [10]. However, in many practical applications the knowledge about the geometry of the spectra is unavailable. For a general multidimensional signal of unknown spectrum, the signal should be sampled as uniformly as possible in order to isotropically preserve high frequencies along all directions [11]. The isotropic treatment of directions suggest the use of a sphere as the shape of an unknown spectrum, which merits the use of sphere packing/covering lattices for sampling general multidimensional signals – even when the signals are not bandlimited. It has been demonstrated that the sphere packing lattices (e.g., FCC) are ideal for sampling rough stochastic processes while their duals (e.g., BCC) are ideal for sampling smooth stochastic processes [11].

While these non-Cartesian lattices have been investigated primarily in the context of regular sampling, in this paper we examine them for bandlimited reconstruction of irregularly sampled data, where the underlying signal has an unknown spectrum. In this setting the sampling positions, X, are placed randomly in space or perturbed from a regular pattern by jitter noise. Our work is motivated by the superiority of the Voronoi cells of BCC/FCC lattices compared to the Voronoi cell of the CC lattice, in terms of the second moments as discussed in the previous section. The smaller moment translates to smaller expected distances which could provide a more accurate reconstruction of the irregularly sampled data.

b) Contributions: In this paper we demonstrate that these seemingly slight differences between the commonly-used

CC and BCC/FCC (aka *optimal*) lattices lead to significant improvement in the accuracy of bandlimited reconstruction. We demonstrate that for a given set of irregularly-sampled data points, the bandlimited reconstruction onto BCC and FCC lattices provide a more accurate reconstruction, when compared to the tensor-product (Cartesian) bandlimited space.

As demonstrated by Conway and Sloane [9], with the increase in dimension, the difference between the normalized moments of the Voronoi cell of the CC lattice and that of the optimal lattices [11] increase significantly with the dimension. Hence the improvements in the accuracy of bandlimited reconstruction compared to the Cartesian reconstruction are expected to generalize to higher dimensions. While for illustration purposes we focus on the 3-D imaging applications, the framework (based on multivariate sinc functions as in Section III) directly generalizes to higher dimensions [12].

II. RELATED WORK

Many applications yield data that are irregularly sampled. For example, simulation datasets in fluid dynamics (e.g., grid-free semi-Lagrangian advection [13]), laser range data (LADAR), and astronomical measurements of star luminosity are sampled irregularly [3]. Biomedical datasets such as magnetic resonance (MR) are often provided to the imaging pipeline on a regular lattice (CC or BCC lattices [14]). However, other trajectories for k-space sampling such as radial and spiral are also sometimes employed by the acquisition system. The acquired data is often resampled to regular lattice for imaging and analysis [15]. Even when the samples are acquired on a regular lattice, the "Eddy currents" and gradient delays in MR may result in perturbation of the sampling locations. This irregularity is often described by jitter noise and the perturbation of the sampling lattice [16].

There are varieties of space domain approaches for reconstruction of irregularly sampled data such as finite element methods [17], radial basis functions [13], [18], [19], moving least squares [20], and natural neighbor interpolation [21], [22]. Moreover various techniques based on B-splines have been proposed for image reconstruction [23], surface reconstruction [24], [25] and volume visualization [26]. In contrast, an entirely different approach has been developed in the non-uniform sampling literature [27] with a sampling theoretic view for reconstruction in bandlimited spaces.

When the data is collected from a single surface (i.e., not the entire volumetric field), surface modeling techniques through PDE-based reconstructions [28] provide direct visualization for scattered data. However, similar to surface reconstruction techniques [29]–[31] the focus is often on reconstruction of a single surface (i.e., moving interfaces, or the object to be modeled). In contrast, we consider the sampling scenario where the samples are taken irregularly from the entire field function. The setting for our approach is to reconstruct the entire volumetric dataset (the 3-D field) simultaneously for all of its iso-surfaces.

Authors have investigated spline fitting of irregularly sampled data in box spline spaces built from CC and BCC lattices [32]. As splines are compactly supported functions in
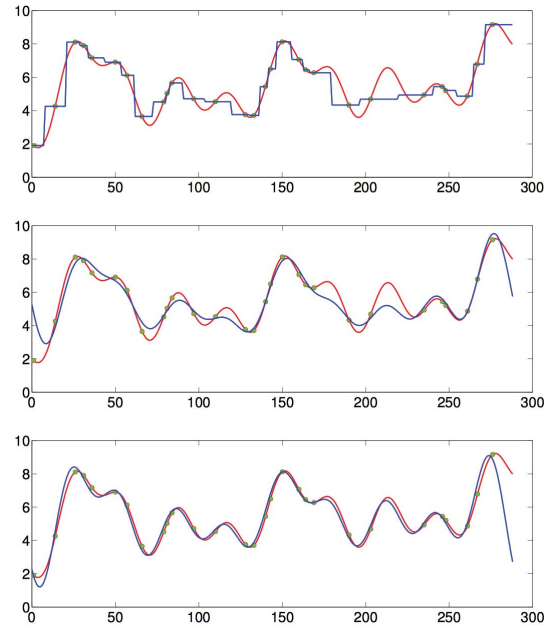

Fig. 3. Allebach algorithm. Given irregular samples (shown in green) of a signal (shown in red), the top, middle and bottom plots show the approximation results (shown in blue) after the initial guess, first iteration and 50th iteration of the Allebach algorithm, respectively.

the space domain, the current paper offers a dual framework which is in the bandlimited setting. The current bandlimited setting allows us to perform a thorough and unbiased analysis of common lattices by including the FCC lattice which is not possible in the spline framework [32]. Moreover, by utilizing sinc functions on these lattices, the frequency response of reconstruction is uniform across all lattices; in contrast box spline's frequency responses differ from CC to BCC lattice [33]. Hence our experiments offer a fair and unbiased analysis of these reconstruction of irregularly sampled data.

A. Non-Uniform Sampling Theory

As illustrated in Fig. 1, the bandlimited reconstruction algorithms in case of irregular sampling try to find the imposed coefficients c_k iteratively. Starting from an initial guess for c_k values, further approximations are obtained, iteratively, by enforcing the interpolation constraint on data f_s and then removing high frequencies – in effect bandlimiting the crude solution that is obtained from the interpolation in the previous iteration. The approximation in each iteration, including the initial guess, is performed by some approximation operator such as nearest neighborhood or polynomial interpolation. For example, the **Allebach algorithm** (also known as the Voronoi method) [27], starts with nearest-neighbor interpolation as the initial guess to coefficients in (1): $c_k^{(0)} = f_i$ where $|k - x_i| \leq |k - x_j|, 1 \leq j \leq N$. Then a filtering step is applied on $c_k^{(0)}$ to remove high frequencies. The filtering can be accomplished in the space domain or by utilizing the Fourier transform (i.e., FFT on the sequence $c_k^{(0)}$) and zeroing frequencies outside the desired bandwidth. The filtering process destroys the interpolation constraint which was enforced by the nearest-neighbor interpolation. This introduces an error

at the (irregular) sampling locations which can be measured directly $e_i^{(0)} = f^{(0)}(x_i) - f_i$. The next iteration, updates the filtered $c_k^{(0)}$ by nearest-neighbor interpolation of errors: $c_k^{(1)} = c_k^{(0)} + e_i^{(0)}$ where $|k - x_i| \leq |k - x_j|, 1 \leq j \leq N$. Since this update destroys the bandlimited property, a filtering process on $c_k^{(1)}$ re-enforces it, and the error $e_i^{(1)}$ is measured. A new iteration then continues to give additive corrections. This iteration is guaranteed to converge at a geometric rate provided the maximal spacing of the sampling set X is smaller than the spacing of Nyquist rate [3]. Fig. 3 illustrates a simple example of the Allebach algorithm. The Allebach algorithm, and its variants (i.e., with different choices of the approximation operator) such as Marvasti algorithm and adaptive weight method converge geometrically with varying rates [27].

These algorithms can also be viewed as iterative solutions to a linear system of equations. Considering (1) for each data point x_i we have a constraint on the c_k sequence: $f_i = \sum_{k \in \mathbb{Z}} c_k \operatorname{sinc}(x_i - k)$. Considering a finite reconstruction domain, one can define $\mathbf{c} := [c_1, \ldots, c_M]^T$ be the set of coefficients covering the reconstruction domain and $\mathbf{f} := [f_1, \ldots, f_N]^T$ be the sampled data values. Defining the $N \times M$ system matrix $\mathbf{S}$ as $\mathbf{S}_{k,i} = \operatorname{sinc}(x_i - k)$ leads to the linear system:

$$\mathbf{f} = \mathbf{S}\,\mathbf{c} \qquad (3)$$

whose solution $\mathbf{c}$ is the coefficients for a bandlimited reconstruction in (1) where the sequence $\mathbf{c}$ is periodically replicated outside of the reconstruction domain. This translates to periodizing sinc function known as the Dirichlet kernel.

The size of the system matrix can be large. Solving the system using direct methods such as applying pseudo-inverse is impractical. Therefore, many iterative methods (e.g., conjugate gradients, Frame iterations, Kaczmarz, randomized Kaczmarz [34]) have been proposed to solve this linear system efficiently [35].

III. MULTIVARIATE SINC FUNCTIONS

As noted earlier, the sinc function for a 1-D lattice ($\mathbb{Z}$) is a function whose Fourier transform is the indicator function of the unit cell of the *dual* lattice $2\pi\mathbb{Z}$: $\chi_{(-\pi,\pi)}(\omega) = 1$ when $|\omega| < \pi$ and $\chi_{(-\pi,\pi)}(\omega) = 0$ when $|\omega| > \pi$.

The notion of duality for higher dimensional lattices involves the generator matrix: the dual (aka reciprocal) to the lattice $\mathbf{L}$ is spanned by $\hat{\mathbf{L}} = 2\pi\mathbf{L}^{-T}$. The CC lattice is self dual; in other words its dual lattice is spanned by the columns of $2\pi\mathbb{C}$. The FCC and BCC lattice are duals of each other upto scaling: the dual to $\mathbb{F}$ is the span of the columns of $2\pi\mathbb{B}$ and the dual to $\mathbb{B}$ is the span of the columns of $2\pi\mathbb{F}$.

Sampling a multidimensional signal, f, on a lattice $\mathbf{L}$ leads to the periodic replication of its Fourier transform, $\hat{f}$, on the dual lattice, $\hat{\mathbf{L}}$. Hence, the unit of replication in the frequency domain (i.e., the Voronoi cell of the dual lattice) is the multidimensional counter part to the $(-\pi, \pi)$ in the univariate sampling theorem as in (1). The Voronoi cell of the dual lattice is called the (first) **Brillouin zone**. In other words, the Brillouin zone is a single unit from the periodic replication on the dual lattice that indicates the maximum
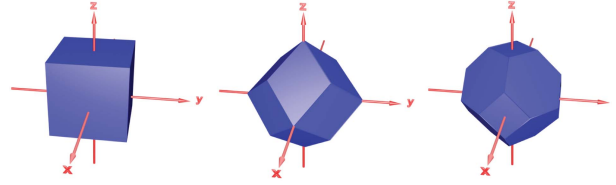

Fig. 4. The Brillouin zone is the multidimensional counter part to the bandwidth interval in the univariate sampling theorem. Brillouin zones of the Cartesian, BCC and FCC lattices are cube, rhombic dodecahedron and truncated octahedron, respectively.

bandwidth (i.e., Nyquist frequency) of a bandlimited signal. Note that the density of a lattice (i.e., sampling density/rate) is equal to the volume of its Brillouin zone but reciprocal to the volume of its Voronoi cell. Similar to the 1-D setting, the sinc function on each lattice is a multivariate function whose Fourier transform is the indicator function of the Brillouin zone. The Brillouin zones of the CC, BCC and FCC lattices are illustrated in Fig. 4.

The Brillouin zone for CC lattice is a cube which makes the integration in the inverse Fourier transform separable and leads to the tensor-product representation of the sinc function:

$$\operatorname{sinc}_{\mathbb{C}}(\mathbf{x}) = \prod_{i=1}^{3} \operatorname{sinc}(\mathbf{e}_i^T \mathbf{x}) = \operatorname{sinc}(x)\operatorname{sinc}(y)\operatorname{sinc}(z) \quad (4)$$

where $\mathbf{x} = [x, y, z]^T$ and $\mathbf{e}_i$ are the canonical axis aligned vectors forming the CC lattice (i.e., columns of $\mathbf{I}$).

The inverse Fourier transforms of Brillouin zones for BCC and FCC are no longer separable which makes the formulas of the sinc functions more involved. However, using the geometric decomposition technique introduced in [12] we can derive the sinc functions for general multidimensional lattices including the BCC and FCC lattices.

The Brillouin zone of the BCC lattice is a rhombic dodecahedron that can be decomposed into 4 parallelohedra. The inverse Fourier transform of the indicator function of each parallelohedron is a product of three sinc functions along the edges of that parallelohedron.

$$\operatorname{sinc}_{\mathbb{B}}(\mathbf{x}) = \frac{1}{4} \sum_{j=1}^{4} [\cos(\pi \xi_j^T \mathbf{x}) \prod_{i \neq j} \operatorname{sinc}(\xi_i^T \mathbf{x})] \quad (5)$$

where

$$[\xi_1 \ldots \xi_4] = \frac{1}{4} \begin{bmatrix} 1 & -1 & -1 & 1 \\ -1 & 1 & -1 & 1 \\ -1 & -1 & 1 & 1 \end{bmatrix} \quad (6)$$

are the principle directions (zones) of the BCC lattice (edges of its Brillouin zone).

The Brillouin zone of the FCC lattice can be decomposed into 16 parallelohedra:

$$\operatorname{sinc}_{\mathbb{F}}(\mathbf{x}) = \frac{1}{16} \sum_{j=1}^{16} [\cos(\pi \mu_j^T \mathbf{x}) \prod_{i \in \mathbf{I}_j} \operatorname{sinc}(\nu_i^T \mathbf{x})] \quad (7)$$

where

$$[v_1 \ldots v_6] = \frac{1}{4} \begin{bmatrix} 1 & -1 & 1 & 1 & 0 & 0 \\ 1 & 1 & 0 & 0 & 1 & -1 \\ 0 & 0 & 1 & -1 & 1 & 1 \end{bmatrix} \quad (8)$$

are the principle directions (zones) of the FCC lattice (edges of its Brillouin zone). The shift vectors μ_j are due to the fact that the parallelepipeds constituting the Brillouin zone of the FCC lattice are shifted from the origin [12].

$$[\mu_1 \ldots \mu_{16}] = \frac{1}{4} \begin{bmatrix} 1 & 3 & 0 & -1 & 2 & 1 & 2 & 0 \\ 0 & -1 & -3 & -1 & 1 & -2 & 0 & 2 \\ 3 & 0 & 1 & 2 & 1 & -1 & -2 & 2 \end{bmatrix}$$
$$\begin{bmatrix} -2 & 1 & 0 & -3 & -2 & -1 & -1 & 0 \\ -2 & 2 & 1 & 0 & 1 & -1 & 3 & 0 \\ 0 & -1 & -3 & -1 & 1 & -2 & 0 & 0 \end{bmatrix}$$

The index set $\mathbf{I}_j$ denotes the edges of jth parallelepiped in truncated octahedron. For example $\mathbf{I}_1 = \{1, 2, 4\}$ indicates that parallelepiped 1 is composed of edges: v_1, v_2 and v_4. Similarly, we have $\mathbf{I}_2 = \{1, 5, 6\}$, $\mathbf{I}_3 = \{3, 4, 5\}$, $\mathbf{I}_4 = \{2, 3, 4\}$, $\mathbf{I}_5 = \{1, 2, 6\}$, $\mathbf{I}_6 = \{3, 5, 6\}$, $\mathbf{I}_7 = \{1, 3, 5\}$, $\mathbf{I}_8 = \{1, 4, 6\}$, $\mathbf{I}_9 = \{2, 4, 5\}$, $\mathbf{I}_{10} = \{1, 2, 3\}$, $\mathbf{I}_{11} = \{1, 2, 5\}$, $\mathbf{I}_{12} = \{4, 5, 6\}$, $\mathbf{I}_{13} = \{3, 4, 6\}$, $\mathbf{I}_{14} = \{2, 5, 6\}$, $\mathbf{I}_{15} = \{1, 3, 4\}$, $\mathbf{I}_{16} = \{2, 3, 6\}$.

In the rest of this paper we refer to the sinc function for a lattice $\mathbf{L}$, as $\text{sinc}_{\mathbf{L}}$ where $\mathbf{L} \in \{\mathbb{C}, \mathbb{B}, \mathbb{F}\}$.

A. Lanczos Window

The support of the sinc function is unbounded which makes its space-domain evaluation impractical. A practical compromise is to truncate the sinc function using a window function. In 1D, there are many windowing techniques such as Hamming, Parzen, Blackman [2]. These window functions can be extended to multivariate CC lattice through tensor-product, but can not be extended to non-tensor-product sinc functions (such as those for BCC and FCC). However, the Lanczos window is defined as the main lobe of the sinc function – a concept that extends to sinc functions defined for any lattice.

Let $S\{\text{sinc}_{\mathbf{L}}\}$ be the support of the main lobe of $\text{sinc}_{\mathbf{L}}$; then, the $\mathcal{L}$anczos windowed $\text{sinc}_{\mathbf{L}}$ is given as:

$$\mathcal{L}(\mathbf{x}) = \begin{cases} \text{sinc}_{\mathbf{L}}(\mathbf{x}) \, \text{sinc}_{\mathbf{L}}^n(\frac{\mathbf{x}}{a}), & \mathbf{x}/a \in S\{\text{sinc}_{\mathbf{L}}\} \\ 0, & \text{otherwise.} \end{cases} \quad (9)$$

where a is the integer valued scaling parameter (usually 2 or 3 in 1-D applications [36]), and determines the size of the window's support. n is the smoothness parameter which controls the degree of continuity of the truncated sinc and how fast the windowed function drops to zero. In this paper, we adopted the choice of $n = 2$ and $a = 3$ as in [12].

B. System Matrix in 3-D

Since the sampled data X is finite, the reconstruction is performed over a finite domain (i.e., the bounding cube in volume visualization). Imposing a (scaled) lattice $\mathbf{L}$ over the domain means only a finite number of lattice points can participate in the reconstruction. In our experiments we have scaled each lattice so that they have the same number of lattice points within the domain of reconstruction. This translates to scaling the Brillouin zones in Fig. 4 to have identical volumes.

Let $\{\mathbf{k}_1, \mathbf{k}_2, \ldots, \mathbf{k}_M\} \in \mathbf{L}\mathbb{Z}^3$ denote the lattice positions that overlap with the bounding cube. For notational convenience, we rename the coefficients $c_m := c_{\mathbf{k}_m}$ from (1) and the lattice shifts of the Lanczos windowed sinc function as $\mathcal{L}_m(\mathbf{x}) := \mathcal{L}(\mathbf{x} - \mathbf{k}_m)$ using this linearized indexing $m = 1 \ldots M$. We then have:

$$f(\mathbf{x}) = \sum_{m=1}^{M} c_m \mathcal{L}_m(\mathbf{x}). \quad (10)$$

Similar to the setup in (3), each data point provides a constraint on the c_m sequence. Let the coefficient (column) vector $\mathbf{c} := [c_1 \cdots c_M]^T$, and the $N \times M$ system matrix whose n^{th} row is the evaluation of $\mathcal{L}_m(\mathbf{x})$ at the sample point $\mathbf{x}_n$: $\mathbf{S}_{m,n} = \mathcal{L}_m(\mathbf{x}_n)$. Then, the interpolation problem, $f(\mathbf{x}_n) = f_n$, for $n = 1 \ldots N$, can be solved by the following linear system:

$$\mathbf{f} = \mathbf{S}\,\mathbf{c}, \quad (11)$$

where $\mathbf{f} := [f_1 \cdots f_N]^T$ are the data values given at the (non-uniform) sample points.

IV. IMPLEMENTATION

According to [3], [37] the Allebach algorithm can be implemented by the conjugate gradient (CG) method which provides a numerically stable method for solving (11) via Normal equations. Depending on the irregularity of the sampling set X, solving (11) is often an under-determined or an over-determined problem. In fact, the non-uniform sampling theory [3], as discussed in Section II-A, requires a cap on the maximum distance between neighboring sample points. In practical applications such a requirement may be violated which, in turn, could lead to rank deficiency of the system in (11). This rank deficiency can be resolved by regularizing the least squares solution obtained by the Normal equation. However, as we intend to compare the solutions built from various lattices, regularizing the discrete coefficients, $\mathbf{c}$, in (11) is biased to the choice of the lattice as the discrete neighborhoods of lattice points are different from each other. As we will see below, our approach regularizes the solution in the *continuous domain* as opposed to regularizing the discrete coefficients in (10).

A. Regularized Least Squares

A classical approach to regularize the least-squares solution is to impose a penalty term to the least-squares fitting process:

$$\min_{\mathbf{c} \in \mathbb{R}^M} \|\mathbf{S}\,\mathbf{c} - \mathbf{f}\|_2^2 + \lambda |f|_H^2. \quad (12)$$

This extra term penalizes unwanted solutions $\mathbf{c}$ that would introduce high oscillations or large energy in the derivative(s) of the solution, $f(\mathbf{x})$ (as in (10)), *in the continuous domain*. The regularization term $|f|_H^2$ is a measure of smoothness and is sensitive to oscillations or large energy in the derivatives of $f(\mathbf{x})$. Tikhonov regularization and total variations impose different types of penalty functions that are often discretized and imposed on the coefficients $\mathbf{c}$. As illustrated below, one can also compute the penalty term over the continuous-domain

$f(\mathbf{x})$ (as opposed to finite differencing on $\mathbf{c}$) and minimize this penalty term over the choices of $\mathbf{c}$. The regularization parameter λ balances the fidelity and smoothness of the solution.

In the 1-D case, the smoothness of a function is often measured by the energy in the second derivative: $|f|^2 = \int (f''(x))^2 dx$, with which the regularized least-squares fitting has a solution that tends to be smooth but with the edge sharpness preserved [38]. In the multidimensional setting, this measure is generalized by measuring the energy of the Laplacian of f [23], [26], [39]:

$$|f|_H^2 = \langle f, f \rangle_H := \langle f_{xx}, f_{xx} \rangle + \langle f_{yy}, f_{yy} \rangle + \langle f_{zz}, f_{zz} \rangle. \tag{13}$$

Here $\langle f, g \rangle = \int f(\mathbf{x})g(\mathbf{x})d\mathbf{x}$ denotes the inner product defined on two functions and the subscript f_{xx} indicates the second partial derivative with respect to x.

Substituting (10) into the Laplacian-based regularization cost function, we have:

$$|f|_H^2 = \langle f, f \rangle_H = \left\langle \sum_{m=1}^{M} c_m \mathcal{L}_m, \sum_{m'=1}^{M} c_{m'} \mathcal{L}_{m'} \right\rangle_H$$
$$= \sum_{m=1}^{M} \sum_{m'=1}^{M} c_m \langle \mathcal{L}_m, \mathcal{L}_{m'} \rangle_H c_{m'} = \mathbf{c}^T \mathbf{G} \mathbf{c}, \tag{14}$$

where each element of the $M \times M$ regularization matrix, $\mathbf{G}$, is the H inner-product between Laplacians of two $\mathcal{L}$ functions shifted to two lattice points:

$$\mathbf{G} := [g_{m,m'}] = \langle \mathcal{L}_m, \mathcal{L}_{m'} \rangle_H \tag{15}$$

For every lattice point the set of neighbors that lead to non-zero inner-products are fixed. Therefore (15) can be pre-computed once for the lattice point at the origin: $\langle \mathcal{L}(\mathbf{x}), \mathcal{L}(\mathbf{x} - \mathbf{k}) \rangle_H$ for the neighboring lattice points $\mathbf{k}$, and re-used for all other lattice points. Since the windowed sinc function $\mathcal{L}$ decays rapidly to zero, only a few neighboring points yield a non-zero inner product. The coefficients computed for lattice neighbors form an FIR filter which leads to a (block) Toeplitz structure for the $\mathbf{G}$ matrix.

B. Optimization

We can now solve (12) by considering the fidelity term in terms of the system matrix:

$$\|\mathbf{Sc} - \mathbf{f}\|_2^2 = \langle \mathbf{Sc} - \mathbf{f}, \mathbf{Sc} - \mathbf{f} \rangle = \mathbf{c}^T \mathbf{S}^T \mathbf{Sc} - 2\mathbf{c}^T \mathbf{S}^T \mathbf{f} + \mathbf{f}^T \mathbf{f},$$

and the regularization term (14):

$$\min_{\mathbf{c} \in \mathbb{R}^M} \mathbf{c}^T \left(\mathbf{S}^T \mathbf{S} + \lambda \mathbf{G} \right) \mathbf{c} - 2\mathbf{c}^T \mathbf{S}^T \mathbf{f}. \tag{16}$$

We can use quadratic programming to solve this minimization process. However, the Hessian of (16), $(\mathbf{S}^T \mathbf{S} + \lambda \mathbf{G})$, is positive definite when the lattice-shifts of the basis functions (i.e., columns of $\mathbf{S}$) are linearly independent [40]. In fact shifts of sinc functions onto their lattice points form an orthonormal set and the windowed sinc functions are nearly orthogonal and hence are linearly independent. Therefore, the unique

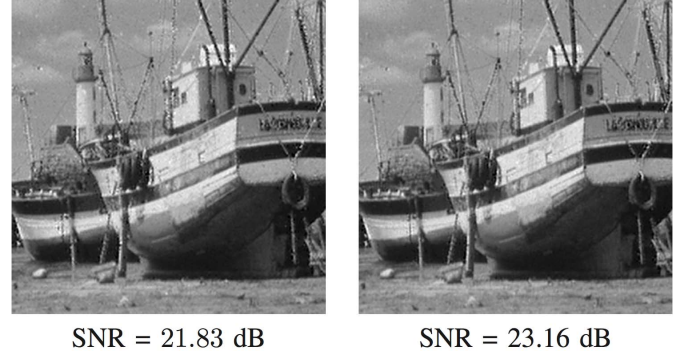SNR = 21.83 dB   SNR = 23.16 dB

Fig. 5.   2-D image reconstruction from 52% ground-truth pixels: Cartesian (left) vs. Hexagonal (right) reconstruction lattice. Regularization parameter $\lambda = 0.001$. The slight increase in accuracy is visible in vertical structures on the top left.

Fig. 6.   3-D imaging of benchmark datasets: A chirp-like 3-D function (synthetic), Aneurysm (MR) and Hydrogen atom (simulation).

minimizer of (16) can be obtained by differentiation with respect to $\mathbf{c}$:

$$\left(\mathbf{S}^T \mathbf{S} + \lambda \mathbf{G} \right) \mathbf{c} = \mathbf{S}^T \mathbf{f}. \tag{17}$$

Since $(\mathbf{S}^T \mathbf{S} + \lambda \mathbf{G})$ is positive definite and symmetric, we can solve (17) efficiently by the conjugate gradient method. The solution to this linear system provides the coefficient vector $\mathbf{c}$ that is used for reconstructing the signal as in (10).

Similar to multi-scaling approach employed in [26] utilizing B-splines, the system matrix corresponding to sinc functions also enjoys from multi-scale properties due to sinc wavelets (Shannon wavelets).

V. EXPERIMENTS

We have examined our separable vs non-separable pipeline in 2-D for image reconstruction from partial pixels. The Cartesian image in Fig. 5 is reconstructed using the tensor-product sinc while the Hexagonal image is reconstructed using the sinc function defined on the Hexagonal lattice. The differences between the separable and the non-separable reconstructions are rather small (about 1 dB) in the 2-D experiments for various test images that we have examined. Fig. 5 illustrates the resulting reconstructions for the boat image where the differences are mostly visible in the background as well as near the vertical structures in the top left.

Our 2-D experiments illustrate a marginal gain from non-separable framework which is in agreement with the small difference between the second moments of a Cartesian pixel vs. a Hexagonal pixel [9]. As we will see next, the advantages of non-separable framework become more significant in the 3-D setting.

TABLE I
NOTATIONS

N	number of irregular samples
M	number of reconstruction lattice points
T	distance between two neighbor points of CC lattice
λ	regularization parameter
$\mathbb{P}_c$	resolution of $41 \times 41 \times 41$ ($M = 68,921$ points)
$\mathbb{P}_b$	resolution of $32 \times 32 \times 32 \times 2$ ($M = 65,536$ points)
$\mathbb{P}_f$	resolution of $25 \times 25 \times 25 \times 4$ ($M = 62,500$ points)
$\mathbf{P}_c$	resolution of $140 \times 140 \times 140$ ($M = 2,744,000$ points)
$\mathbf{P}_b$	resolution of $111 \times 111 \times 111 \times 2$ ($M = 2,735,262$ points)
$\mathbf{P}_f$	resolution of $88 \times 88 \times 88 \times 4$ ($M = 2,725,888$ points)

In what follows, we investigate the visual and numerical accuracy of reconstruction onto the 3-D sampling lattices along with non-separable basis functions. We compare the accuracy of the reconstruction results returned by the corresponding CC, BCC and FCC lattices of equivalent density.

A. Experiment Setting in 3-D

We experiment with both synthetic and real volumetric datasets (see Fig. 6 and Fig. 9). Our synthetic benchmark is a chirp-like frequency-modulation dataset proposed by Marschner and Lobb (ML) [41] (see Section V-B). Sample values of the ML dataset can be evaluated by the explicit function described in [41]. Our experiments on real volumetric datasets (see Section V-C) involve both biomedical datasets and scientific simulation datasets. We use the Carp Fish (CT), Aneurysm (MR) and Hydrogen (simulation) datasets[1]. Note that the Carp Fish and Aneurysm datasets are somewhat noisy due to the acquisition process.

To ensure the CC, BCC and FCC lattices (superimposed on the irregular dataset) have the same lattice densities within the domain, we scale the lattices so that the volumes of their Voronoi cells (i.e., cube, truncated octahedron and rhombic dodecahedron, respectively) are equal. Note that over a finite domain we may not be able to contain the exact same number of lattice points for the three lattice patterns with the same lattice density. To be conservative in our experiments, we pick resolutions in favor of the CC lattice as shown below. Therefore inside the domain, the CC lattice could have slightly more lattice points than the BCC and FCC lattices. The reported advantages of the latter are despite the slight resolution advantages that we give to the CC lattice.

For brevity of discussion, we have defined several notations for the rest of paper, as summarized in Table I. For our experiments on the synthetic dataset, ML, we denote the resolutions of the CC, BCC and FCC reconstruction lattices as $\mathbb{P}_c$, $\mathbb{P}_b$ and $\mathbb{P}_f$, respectively[2]. This resolution is a "practical" Nyquist frequency for ML [41]. For real datasets, the superimposed CC lattice has a fixed resolution of $\mathbf{P}_c$ while the BCC and FCC lattices have the resolution of $\mathbf{P}_b$ and $\mathbf{P}_f$, respectively. In other words, we fix the number of imposed reconstruction lattice points (i.e., M), and examine the performance of three

[1]Courtesy of http://www9.informatik.uni-erlangen.de/External/vollib/.

[2]The BCC lattice can be considered as two interleaving CC lattices, while the FCC lattice can be considered as four interleaving CC lattices.
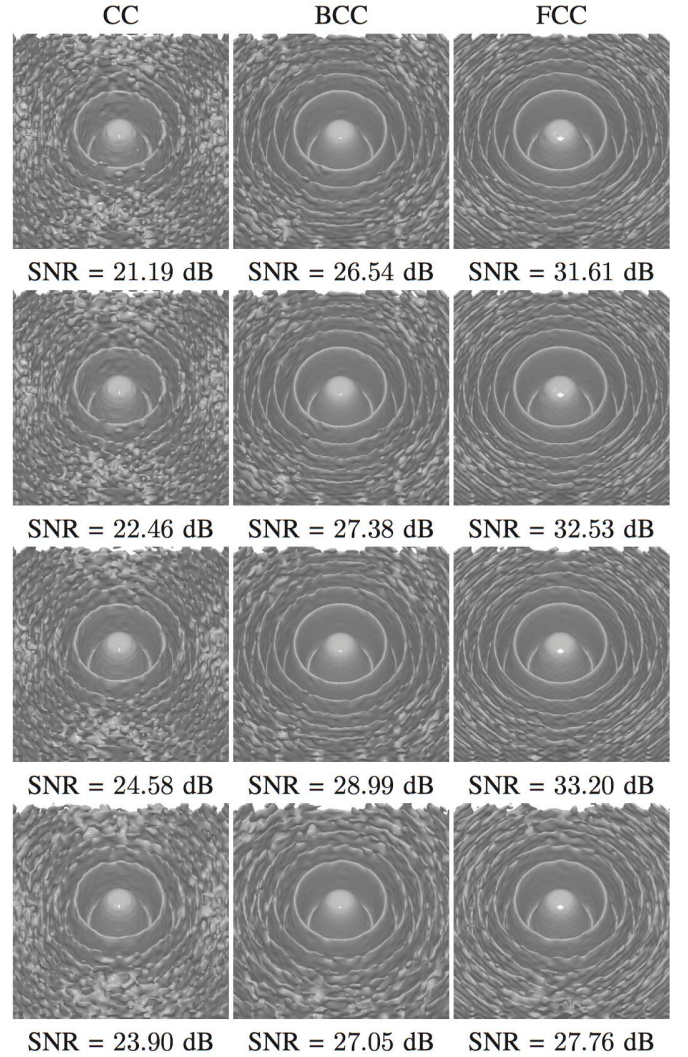

Fig. 7. Reconstruction of the ML dataset from $N = 1.5M$ random samples. Resolution of the CC (first column), BCC (second column) and FCC (third column) reconstruction lattices are $M = \mathbb{P}_c$, $\mathbb{P}_b$ and $\mathbb{P}_f$, respectively. Regularization parameter $\lambda = 0$ (first row), $\lambda = 1 \times 10^{-4}$ (second row), $\lambda = 1 \times 10^{-3}$ (third row) and $\lambda = 1 \times 10^{-2}$ (fourth row).

lattices when the number of irregular samples (i.e., N) or regularization parameter (i.e., λ) or jitter noise level are varied.

All images are rendered by a ray-caster from the reconstructed volumetric images. To avoid clutter in the images, single iso-surfaces are extracted from the volume, in the rendering stage, so that the images can be visually compared. The reconstruction accuracy is measured quantitatively by the SNR (Signal to Noise Ratio). We note that the SNR's are always computed over the entire volumetric domain and is not limited to the rendered iso-surfaces.

B. Synthetic Dataset

Fig. 7 illustrates the reconstruction from $N = 1.5M$ irregular ML samples. Samples are placed inside the bounding domain randomly with a uniform distribution. Since we want to give the same data points to each of the CC, BCC and FCC reconstruction pipelines, we fixed the configuration of the irregular sampling points according to $N = 1.5\mathbb{P}_c$ for the
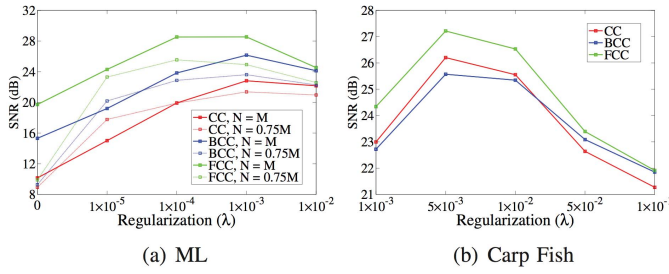
(a) ML   (b) Carp Fish

Fig. 8. Reconstruction from irregular samples. (a) The ML dataset reconstructed from $N = 0.75M$ (dash lines) and $N = M$ (solid lines) irregular samples. Resolution of the CC (red lines), BCC (blue lines) and FCC (green lines) lattices are $M = \mathbb{P}_c$, $\mathbb{P}_b$ and $\mathbb{P}_f$, respectively. (b) The carp fish dataset reconstructed from $N = 800,000$ irregular samples. Resolution of the CC (red line), BCC (blue line) and FCC (green line) lattices are $\mathbf{P}_c$, $\mathbf{P}_b$ and $\mathbf{P}_f$, respectively. The SNR underestimates the advantages of BCC/FCC (also see Fig. 9), which is influenced by the existing noise in the underlying dataset.

Cartesian lattice and used the same sampled data for BCC and FCC (and picked their respective M to $M = \mathbb{P}_b$ and $M = \mathbb{P}_f$).

On each row (i.e., for a fixed λ) of Fig. 7, we can clearly see that the BCC and FCC lattices outperform the CC by 5 and 10 dB's, and FCC wins among the latter two. Each column corresponds to reconstruction onto one lattice with varying value of the regularization parameter. We can see that the regularization can improve the reconstruction performance. As λ increases, the reconstruction accuracy increases to a certain level (i.e., $\lambda = 1 \times 10^{-3}$ in this cases), and then drops. This reflects the compromise between the fitting accuracy and the smoothness of the solution. Although picking the best λ is not straightforward, the regularization parameter affects the three lattices uniformly. This is due to the fact that we are regularizing the continuous-domain solution, not the discrete lattice coefficients.

Obvious artifacts of CC reconstruction can be seen on the inner three rings of the dataset, while they are reconstructed with high accuracy on BCC and FCC reconstruction. Reconstruction of high frequency parts of ML dataset (i.e., outer rings) fails on CC reconstruction, however, BCC and FCC reconstruction can preserve those parts more accurately.

Fig. 8(a) plots SNR results of reconstruction of ML dataset from smaller number of irregular samples ($N = 0.75M$ and M). The regularization improves the reconstruction performance, especially when the system matrix (i.e., $\mathbf{S}$ in (11)) is under-determined, that is, when we have fewer samples than the reconstruction lattice points. Experimenting with different numbers of irregular samples (see Fig. 7 and Fig. 8(a)), we observe that the BCC and FCC lattices consistently outperform the CC lattice across various levels of regularizations.

C. Real Datasets

Fig. 8(b) plots the reconstruction accuracy for the carp fish from an irregularly-sampled dataset with $N = 800,000$. The irregular samples are generated by randomly picking points from the ground truth dataset with a resolution of $256 \times 256 \times 256$. We adopt an adaptive sampling strategy [3] such that a point/sample is picked with a probability proportional to the magnitude of the gradient at that point. Without regularization
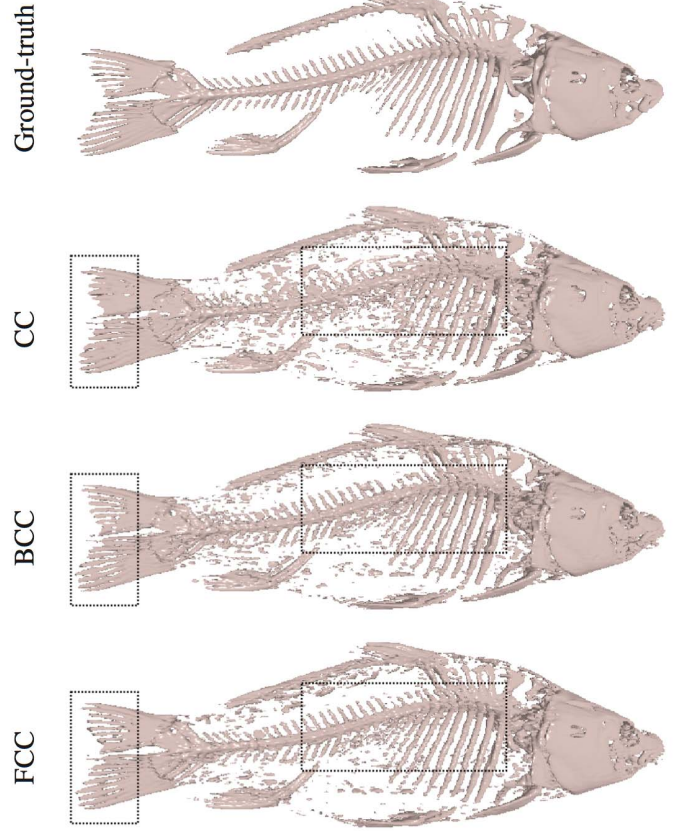

Fig. 9. Rendering of Carp fish (CT dataset) corresponding to the cases of $\lambda = 1 \times 10^{-3}$ in Fig. 8(b). The top image shows the ground-truth. The SNR values of CC (second row), BCC (third row) and FCC (bottom row) reconstruction are 22.99 dB, 22.72 dB and 24.34 dB, respectively. The tail fins and ribs areas (dotted boxes) are reconstructed more accurately on the FCC and BCC compared to the CC. The SNR values underestimate the advantages of BCC and FCC because of existing noise in the background of the CT dataset.

(i.e., $\lambda = 0$, not shown in the plot), the reconstruction fails (yielding SNR of 0.1406 dB, 2.2083 dB and 2.2755 dB for CC, BCC and FCC, respectively) as the system matrix is severely under-determined.

Fig. 9 is the rendering result of the case of $\lambda = 1 \times 10^{-3}$ in Fig. 8(b). The precision of reconstruction can be easily observed from tail fins and ribs of the fish (see dotted boxes). The CC approximation (second row) merges the tail fins, while the BCC and FCC (the third and fourth rows) preserve them. BCC and FCC approximation keep the individual structure of each rib clear, however reconstruction onto the CC lattice has additional artifacts merging neighboring ribs. In general BCC and FCC lattices yield a cleaner reconstruction than CC lattice. The SNR values underestimate the performance of BCC and FCC cases since the values are computed over the entire volume including noisy areas that are away from the irregularly picked samples.

D. Resilience to Jitter Noise

In statistical physics, structural stability of CC, BCC and FCC lattices are studied for the impact of jitter noise [42].
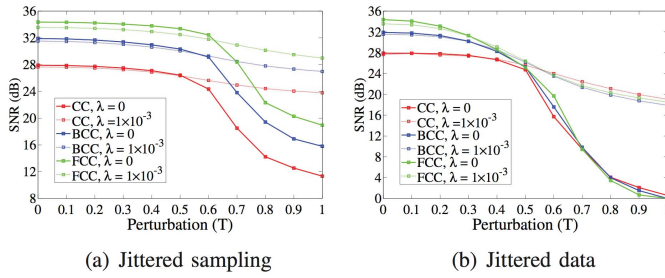
(a) Jittered sampling   (b) Jittered data

Fig. 10.   Reconstruction of the ML dataset from $N = M$ samples using CC ($M = \mathbb{P}_c$, red lines), BCC ($M = \mathbb{P}_b$, blue lines) and FCC ($M = \mathbb{P}_f$, green lines) reconstruction lattice. (a) Jittered sampling. (b) Jittered data.
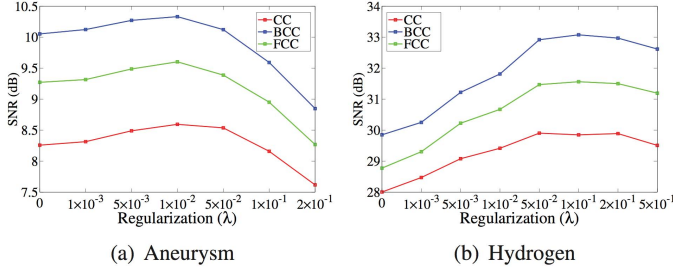

(a) Aneurysm   (b) Hydrogen

Fig. 11.   Jittered data. (a) Reconstruction of the Aneurysm dataset from $N = M$ samples using CC ($M = \mathbf{P}_c$, red lines), BCC ($M = \mathbf{P}_b$, blue lines) and FCC ($M = \mathbf{P}_f$, green lines) reconstruction lattice. The maximum radius of the perturbation is $0.25 \times T$. (b) Reconstruction of the Hydrogen dataset from $N = M$ samples using CC ($M = \mathbf{P}_c$, red lines), BCC ($M = \mathbf{P}_b$, blue lines) and FCC ($M = \mathbf{P}_f$, green lines) reconstruction lattice. The maximum radius of the perturbation is $0.5 \times T$.

In the following experiments, we study the impact of jitter noise on the quality of sampling and reconstruction in our bandlimited reconstruction framework and experiment the resilience of these lattices against jitter noise.

We introduce a *jittered sampling* experiment and a *jittered data* experiment. To generate irregular samples for jittered sampling experiments, we choose a sampling lattice **L**, perturb the location of each lattice point of **L** randomly, and then sample the ground-truth signal at the perturbed position. In contrast, for jittered data experiments, the irregular samples come from sampling at the lattice points and perturbing the data location after the sampling process. In both cases, the irregularity of sample set is controlled by the maximum radius of the perturbation (e.g., $0.5T$, where T is defined in Table I). As described in Section II, the jittered sampling and jittered data can happen in the process of acquisition data (e.g., medical modalities or LADAR data). When reconstructing from irregular samples, we choose the superimposed reconstruction lattice the same as **L**, that is, we have $N = M$.

Fig. 10(a) plots the performance of CC, BCC and FCC lattices with varying radii of perturbation on sampling lattices (i.e., jittered sampling). These experiments demonstrate that the BCC and FCC lattices consistently outperform the CC lattice with varying irregularity of the sampling lattices. Fig. 10(b) plots the results of our jittered data experiments. We can see that within certain range of perturbation of the sampled data (e.g., the perturbation is less than $0.4T$), BCC and FCC lattices have better reconstruction results than CC lattice. However, as the perturbation goes up, the performance of three

SNR = 8.54 dB   SNR = 7.62 dB

SNR = 10.12 dB   SNR = 8.85 dB
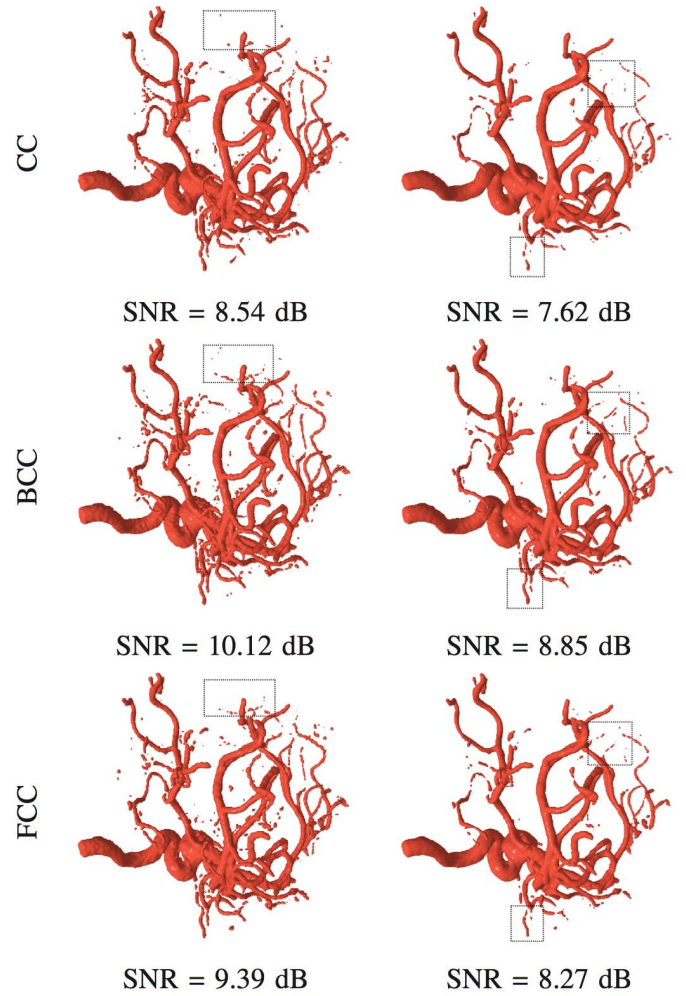
SNR = 9.39 dB   SNR = 8.27 dB

Fig. 12.   Rendering of Aneurysm (MR angiography) dataset with the reconstruction setup corresponding to the cases of $\lambda = 0.05$ (left column) and $\lambda = 0.2$ (right column) in Fig. 11(a).

lattices drop down to a similar level. With regularization, the CC lattice even yields slightly better results than BCC and FCC lattices for the perturbation larger than $0.6T$.

Fig. 10(b) shows quite a different pattern from Fig. 10(a). In jittered sampling (Fig. 10(a)), the perturbation (on sampling lattice) is done before sampling the signal, and thus provides non-uniform samples of the signal. However, in jittered data (Fig. 10(b)), the already regularly-sampled data is perturbed to a nearby location, and the data value is treated as the signal value at that location. For jittered data case, beyond certain level of perturbation (e.g. $0.5T$), the provided irregular samples become highly unreliable for reconstruction, vanishing the advantages of BCC and FCC reconstruction. Both Fig. 10(a) and Fig. 10(b) show that the regularization leads to a slow drop in performance when the perturbation is severe.

Fig. 11(a) and Fig. 12 illustrate the accuracy of reconstruction of the Aneurysm dataset from jittered data (i.e., perturbation of regularly-sampled data). From Fig. 11(a), we see that FCC and BCC reconstruction yield around 1 and 2 dB higher SNR's than CC reconstruction, respectively. All SNR values are relatively low because the dataset is noisy
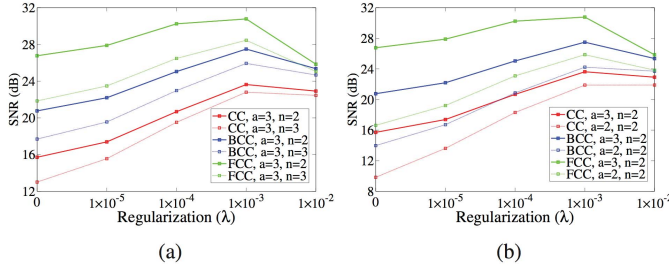
Fig. 13. Reconstruction of ML dataset from $N = 1.2M$ irregular samples. Resolution of the CC (red lines), BCC (blue lines) and FCC (green lines) lattices are $M = \mathbb{P}_c$, $\mathbb{P}_b$ and $\mathbb{P}_f$, respectively. (a) Solid lines are results from kernel with $a = 3$ and $n = 2$, while dotted lines are with $a = 3$ and $n = 3$. (b) Solid lines are results from kernel with $a = 3$ and $n = 2$, while dotted lines are with $a = 2$ and $n = 2$.

and structures are contained in a very small region of the volume. The reconstruction difference can also be seen from Fig. 12, where the rendered datasets correspond to the cases of $\lambda = 0.05$ and $\lambda = 0.2$ in Fig. 11(a). The dotted boxes highlight areas where thin veins are absent with CC lattice while BCC and FCC still preserve these veins, which indicates a higher SNR in those regions.

Fig. 11(b) is the experiment on reconstructing a simulation (Hydrogen atom) dataset from jittered data. We achieve high reconstruction SNR's (i.e., more than 28 dB). We can see that compared to CC lattice, BCC and FCC lattice are more resilient to jitter noise.

E. Lanczos Windowed sinc_L Parameters

We have already described in Section III-A that the Lanczos windowed sinc_L involves two parameters, a and n, where a determines the size of the kernel support, and n controls the degree of continuity of the windowed sinc. In our previous 3-D experiments, we have used $a = 3$ and $n = 2$.

Fig. 13 is the SNR results of reconstruction from $N = 1.2M$ random ML samples with different parameter settings of the windowed sinc. The solid lines in both figures are our comparison basis with the same kernel parameter settings as the experiments shown in the previous sections. Dotted lines in Fig. 13(a) show the results with $a = 3$ and $n = 3$, and dotted lines in Fig. 13(b) are for the case of $a = 2$ and $n = 2$. We can see that increasing the kernel function continuity (see Fig. 13(a)) decreases the reconstruction accuracy because the kernel over-smooths the high frequency parts of the signal. Smaller window size (see Fig. 13(b)) also decreases the performance since fewer samples are used for reconstruction. However, we can observe from these plots that the reconstructions from BCC and FCC lattices still outperform those of the CC lattice among various kernel settings.

F. Computational Cost

The main workload of our framework is to find the solution of the linear system (17), where the conjugate gradient method is used in our experiments. Iterative methods such as conjugate gradient method are particularly efficient when the linear system has sparse matrix (i.e., $\left(\mathbf{S}^T\mathbf{S} + \lambda\mathbf{G}\right)$ in our

case), which is the case in our framework. In addition, as mentioned in Section IV, the regularization matrix G can be pre-computed and re-used. Therefore, our reconstruction framework is efficient and practical.

Our experiments were carried out on a desktop with a single core 2.20GHz CPU. We implemented a solver for (17) using MATLAB's built-in conjugate gradient method and the CG method converged within 200 iterations. In our experiments, the solver returned within 30 minutes. The reconstruction time can be significantly shortened with more powerful machines (e.g., multi-core) and parallelization techniques.

We also observe that, with the same parameter setting, reconstruction onto the BCC and FCC lattices require less time to solve the system (17) than reconstruction onto the CC lattice. This is because that the Lanczos Windowed sinc_L functions corresponding to the BCC and FCC lattices have smaller support compared to CC one. The system matrices $\mathbf{S}$ for the BCC and FCC cases are then sparser than the CC case, which in turn reduces the computational cost of numerical methods taking advantage of sparsity, such as the conjugate gradient method.

VI. CONCLUSION

This paper provides a framework for bandlimited reconstruction of multidimensional images from irregularly sampled data using optimal sampling lattices. The approach uses the sinc functions defined over these lattices and can be considered as an extension of the Allebach algorithm to the multidimensional setting. Through numerical and visual comparisons we established that for a given set of sampled data the optimal sampling lattices along with non-separable sinc functions provide a more accurate reconstruction than the Cartesian lattice with the tensor-product sinc function. The gain from the non-separable framework is much more significant (up to ~ 10 dB) in 3-D compared to 2-D (~ 1 dB) which agrees with the theoretical expectations that the efficiency of optimal lattices increase in higher dimensions.

REFERENCES

[1] M. Unser, "Sampling-50 years after shannon," *Proc. IEEE*, vol. 88, no. 4, pp. 569–587, Apr. 2000.

[2] A. Oppenheim and R. Schafer, *Discrete-Time Signal Processing*. Saddle River, NJ, USA: Prentice-Hall, 1989.

[3] A. Aldroubi and K. Gröchenig, "Nonuniform sampling and reconstruction in shift-invariant spaces," *SIAM Rev.*, vol. 43, no. 4, pp. 585–620, 2001.

[4] H. Miyakawa, "Sampling theorem of stationary stochastic variables in multidimensional space," *J. Inst. Electron. Commun. Eng. Jpn.*, vol. 42, pp. 421–427, Jan. 1959.

[5] D. P. Petersen and D. Middleton, "Sampling and reconstruction of wave-number-limited functions in N-dimensional Euclidean spaces," *Inf. Control*, vol. 5, no. 4, pp. 279–323, Dec. 1962.

[6] D. Van De Ville, T. Blu, M. Unser, W. Philips, I. Lemahieu, and R. Van de Walle, "Hex-splines: A novel spline family for hexagonal lattices," *IEEE Trans. Image Process.*, vol. 13, no. 6, pp. 758–772, Jun. 2004.

[7] D. E. Dudgeon and R. M. Mersereau, *Multidimensional Digital Signal Processing*, 1st ed. Englewood-Cliffs, NJ, USA: Prentice-Hall, 1984.

[8] A. Entezari, "Optimal sampling lattices and trivariate box splines," Ph.D. dissertation, Dept. Comput. Sci., Simon Fraser Univ., Vancouver, Canada, Jul. 2007.

[9] J. Conway and N. Sloane, *Sphere Packings, Lattices and Groups*, 3rd ed. New York, NY, USA: Springer-Verlag, 1999.

[10] Y. M. Lu, M. N. Do, and R. S. Laugesen, "A computable fourier condition generating alias-free sampling lattices," *IEEE Trans. Signal Process.*, vol. 57, no. 5, pp. 1768–1782, May 2009.

[11] H. Kunsch, E. Agrell, and F. Hamprecht, "Optimal lattices for sampling," *IEEE Trans. Inf. Theory*, vol. 51, no. 2, pp. 634–647, Feb. 2005.

[12] W. Ye and A. Entezari, "A geometric construction of multivariate sinc functions," *IEEE Trans. Image Process.*, vol. 21, no. 6, pp. 2969–2979, Jun. 2012.

[13] H. Wendland, *Scattered Data Approximation*, vol. 17. Cambridge, U.K.: Cambridge Univ. Press, 2005.

[14] M. Saranathan, V. Ramanan, R. Gulati, and R. Venkatesan, "ANTHEM: Anatomically tailored hexagonal MRI," *Magn. Resonance Imag.*, vol. 25, no. 7, pp. 1039–1047, 2007.

[15] W. Ye, A. Entezari, and B. Vemuri, "Tomographic reconstruction of diffusion propagators from dw-mri using optimal sampling lattices," in *Proc. IEEE Int. Symp. Biomed. Imag., Nano Macro*, Apr. 2010, pp. 788–791.

[16] M. Tisdall, "Development and validation of algorithms for MRI signal component estimation," Ph.D. dissertation, Dept. Comput. Sci., Simon Fraser Univ., Vancouver, Canada, Dec. 2007.

[17] J. R. Shewchuk, "What is a good linear element?-interpolation, conditioning, and quality measures," in *Proc. Conf. Proc. 11th Int. Meshing Roundtable*, Sep. 2002, pp. 115–126.

[18] G. M. Nielson, "Scattered data modeling," *IEEE Comput. Graph. Appl.*, vol. 13, no. 1, pp. 60–70, Jan. 1993.

[19] Y. Jang, R. Botchen, A. Lauser, D. Ebert, K. Gaither, and T. Ertl, "Enhancing the interactive visualization of procedurally encoded multifield data with ellipsoidal basis functions," *Comput. Graph. Forum*, vol. 25, no. 3, pp. 587–596, 2006.

[20] C. Ledergerber, G. Guennebaud, M. Meyer, M. Bacher, and H. Pfister, "Volume MLS ray casting," *IEEE Trans. Vis. Comput. Graph.*, vol. 14, no. 6, pp. 1372–1379, Nov. 2008.

[21] S. W. Park, L. Linsen, O. Kreylos, J. D. Owens, and B. Hamann, "Discrete sibson interpolation," *IEEE Trans. Vis. Comput. Graph.*, vol. 12, no. 2, pp. 243–253, Mar. 2006.

[22] T. Bobach, G. Farin, D. Hansford, and G. Umlauf, "Natural neighbor extrapolation using ghost points," *Comput. Aided Design*, vol. 41, no. 5, pp. 350–365, 2009.

[23] M. Arigovindan, M. Suhling, P. Hunziker, and M. Unser, "Variational image reconstruction from arbitrarily spaced samples: A fast multiresolution spline solution," *IEEE Trans. Image Process.*, vol. 14, no. 4, pp. 450–460, Apr. 2005.

[24] B. Gregorski, B. Hamann, and K. Joy, "Reconstruction of B-spline surfaces from scattered data points," in *Proc. Comput. Graph. Int.*, 2000, pp. 163–170.

[25] S. Lee, G. Wolberg, and S. Shin, "Scattered data interpolation with multilevel B-splines," *IEEE Trans. Vis. Comput. Graph.*, vol. 3, no. 3, pp. 228–244, Jul. 1997.

[26] E. Vuçini, T. Möller, and M. Gröller, "Efficient reconstruction from nonuniform point sets," *Vis. Comput.*, vol. 24, no. 7, pp. 555–563, 2008.

[27] F. Marvasti, *Nonuniform Sampling: Theory and Practice*, vol. 1. New York, NY, USA: Springer-Verlag, 2001.

[28] P. Rosenthal, V. Molchanov, and L. Linsen, "A narrow band level set method for surface extraction from unstructured point-based volume data," in *Proc. 18th WSCG*, 2010, pp. 73–80.

[29] M. Pauly, R. Keiser, L. Kobbelt, and M. Gross, "Shape modeling with point-sampled geometry," *ACM Trans. Graph.*, vol. 22, no. 3, pp. 641–650, 2003.

[30] H. Hoppe, T. DeRose, T. Duchamp, J. McDonald, and W. Stuetzle, *Surface Reconstruction from Unorganized Points*. Seattle, WA, USA: Citeseer, 1994.

[31] M. Zwicker, M. Pauly, O. Knoll, and M. Gross, "Pointshop 3D: An interactive system for point-based surface editing," in *Proc. 29th Annu. Conf. Comput. Graph. Interact. Tech.*, 2002, pp. 322–329.

[32] X. Xu, A. Alvarado, and A. Entezari, "Reconstruction of irregularly-sampled volumetric data in efficient box spline spaces," *IEEE Trans. Med. Imag.*, vol. 31, no. 7, pp. 1472–1480, Jul. 2012.

[33] A. Entezari, D. Van De Ville, and T. Möller, "Practical box splines for reconstruction on the body centered cubic lattice," *IEEE Trans. Vis. Comput. Graph.*, vol. 14, no. 2, pp. 313–328, Mar.–Apr. 2008.

[34] T. Strohmer and R. Vershynin, "A randomized Kaczmarz algorithm with exponential convergence," *J. Fourier Anal. Appl.*, vol. 15, no. 2, pp. 262–278, 2009.

[35] T. Strohmer and J. Tanner, "Fast reconstruction methods for bandlimited functions from periodic nonuniform sampling," *SIAM J. Numer. Anal.*, vol. 44, pp. 1073–1094, Mar. 2006.

[36] J. Blinn, *Jim Blinn's Corner: Dirty Pixels*. San Francisco, CA, USA: Morgan Kaufmann Publishers Inc., 1998.

[37] H. G. Feichtinger, K. Gröchenig, and T. Strohmer, "Efficient numerical methods in non-uniform sampling theory," *Numer. Math.*, vol. 69, pp. 423–440, Feb. 1995.

[38] W. Zhu, Y. Wang, and Q. F. Zhu, "Second-order derivative-based smoothness measure for error concealment in DCT-based codecs," *IEEE Trans. Circuits Syst. Video Technol.*, vol. 8, no. 6, pp. 713–718, Oct. 1998.

[39] O. Morozov, M. Unser, and P. Hunziker, "Reconstruction of large, irregularly sampled multidimensional images. A tensor-based approach," *IEEE Trans. Med. Imag.*, vol. 30, no. 2, pp. 366–374, Feb. 2011.

[40] M. Johnson, Z. Shen, and Y. Xu, "Scattered data reconstruction by regularization in B-spline and associated wavelet spaces," *J. Approx. Theory*, vol. 159, no. 2, pp. 197–223, 2009.

[41] S. R. Marschner and R. J. Lobb, "An evaluation of reconstruction filters for volume rendering," in *Proc. IEEE Conf. Visualizat.*, Oct. 1994, pp. 100–107.

[42] V. Lucarini, "Three-dimensional random Voronoi tessellations: From cubic crystal lattices to poisson point processes," *J. Stat. Phys.*, vol. 134, no. 1, pp. 185–206, 2009.
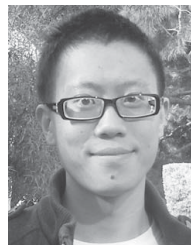
Xie Xu received the B.E. degree in software engineering from Tianjin University, Tianjin, China, in 2009. He is currently pursuing the Ph.D. degree with the Department of Computer and Information Science and Engineering, University of Florida, Gainesville, FL, USA.

His current research interests include signal processing, compressed sensing, and scientific visualization.
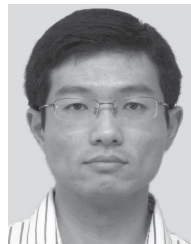
Wenxing Ye received the Ph.D. degree from the Department of Electrical and Computer Engineering, University of Florida, Gainesville, FL, USA, in 2012, and the B.E. degree from the Department of Automation, University of Science and Technology of China, Hefei, China, in 2004. He is currently with Google Inc.

His current research interests include multidimensional signal processing, image analysis, medical imaging, and machine learning.

Alireza Entezari (M'–) received the Ph.D. degree from the School of Computing Science, Simon Fraser University, Vancouver, BC, Canada, in 2007.

He is currently an Assistant Professor with the Computer and Information Science and Engineering Department, University of Florida, Gainesville, FL, USA. He has co-organized a workshop on sampling and reconstruction at Banff International Research Station in 2010. His current research interests include multidimensional signal processing and multivariate splines, with particular applications in scientific visualization and biomedical imaging.